# THE ROLE OF SHABANSKY ORBITS IN COMPRESSION-RELATED ELECTROMAGNETIC ION CYCLOTRON WAVE GROWTH (POSTPRINT)

J. P. McCollough, et al.

**15 March 2012**

**Technical Paper**

APPROVED FOR PUBLIC RELEASE; DISTRIBUTION IS UNLIMITED.

**AIR FORCE RESEARCH LABORATORY**
**Space Vehicles Directorate**
**3550 Aberdeen Ave SE**
**AIR FORCE MATERIEL COMMAND**
**KIRTLAND AIR FORCE BASE, NM 87117-5776**

# REPORT DOCUMENTATION PAGE

*Form Approved*
*OMB No. 0704-0188*

Public reporting burden for this collection of information is estimated to average 1 hour per response, including the time for reviewing instructions, searching existing data sources, gathering and maintaining the data needed, and completing and reviewing this collection of information. Send comments regarding this burden estimate or any other aspect of this collection of information, including suggestions for reducing this burden to Department of Defense, Washington Headquarters Services, Directorate for Information Operations and Reports (0704-0188), 1215 Jefferson Davis Highway, Suite 1204, Arlington, VA 22202-4302. Respondents should be aware that notwithstanding any other provision of law, no person shall be subject to any penalty for failing to comply with a collection of information if it does not display a currently valid OMB control number. **PLEASE DO NOT RETURN YOUR FORM TO THE ABOVE ADDRESS.**

| 1. REPORT DATE *(DD-MM-YYYY)*<br>15-03-2012 | 2. REPORT TYPE<br>Technical Paper | 3. DATES COVERED *(From - To)*<br>01 Apr 2007 − 10 Nov 2011 |
|---|---|---|

| 4. TITLE AND SUBTITLE<br><br>The role of Shabansky orbits in compression-related electromagnetic ion cyclotron wave growth (Postprint) | 5a. CONTRACT NUMBER |
|---|---|
| | 5b. GRANT NUMBER |
| | 5c. PROGRAM ELEMENT NUMBER<br>62601F |
| 6. AUTHOR(S)<br><br>J. P. McCollough, S. R. Elkington, and D. N. Baker | 5d. PROJECT NUMBER<br>1010 |
| | 5e. TASK NUMBER<br>PPM00004260 |
| | 5f. WORK UNIT NUMBER<br>EF004414 |

| 7. PERFORMING ORGANIZATION NAME(S) AND ADDRESS(ES)<br><br>Air Force Research Laboratory<br>Space Vehicles Directorate<br>3550 Aberdeen Ave. SE<br>Kirtland AFB, NM 87117-5776 | 8. PERFORMING ORGANIZATION REPORT NUMBER<br><br>AFRL-RV-PS-TP-2012-0023 |
|---|---|

| 9. SPONSORING / MONITORING AGENCY NAME(S) AND ADDRESS(ES) | 10. SPONSOR/MONITOR'S ACRONYM(S)<br><br>AFRL/RVBXR |
|---|---|
| | 11. SPONSOR/MONITOR'S REPORT NUMBER(S) |

**12. DISTRIBUTION / AVAILABILITY STATEMENT**

Approved for public release; distribution is unlimited. (377ABW-2011-0962 dtd 23 Jun 2011)

**14. ABSTRACT**
Electromagnetic ion cyclotron waves at high L values near local noon are often found to be related to magnetospheric compression events. These waves arise from temperature anisotropies in trapped warm plasma populations. There are several possible mechanisms that can generate these temperature anisotropies, including both energizing and nonenergizing processes. In this work we investigate a nonenergizing process arising from dayside bifurcated magnetic field minima. There are two kinds of behavior particles undergo in the presence of bifurcated minima: particles with high initial equatorial pitch angles (EPAs) are forced to execute so-called Shabansky orbits and mirror at high latitudes without passing through the equator, while those with lower initial EPAs will pass through the equator with higher EPAs than before; as a result, perpendicular energies near the equator increase at the cost of parallel energies. By using a 3-D particle tracing code in a tunable analytic compressed-dipole field, we explore the effects of Shabansky orbits on the anisotropy of the warm plasma and contrast with the anisotropy resulting from drift shell splitting. We show that Shabansky orbits are an independent source of temperature anisotropy for warm dayside ions.

**15. SUBJECT TERMS**
Shabansky orbits, equatorial pitch angles, electromagnetic ion cyclotron waves, drift shell splitting

| 16. SECURITY CLASSIFICATION OF: | | | 17. LIMITATION OF ABSTRACT | 18. NUMBER OF PAGES | 19a. NAME OF RESPONSIBLE PERSON<br>Adrian Wheelock |
|---|---|---|---|---|---|
| a. REPORT<br>Unclassified | b. ABSTRACT<br>Unclassified | c. THIS PAGE<br>Unclassified | Unlimited | 16 | 19b. TELEPHONE NUMBER *(include area code)* |

**Standard Form 298 (Rev. 8-98)**
Prescribed by ANSI Std. 239.18

# The role of Shabansky orbits in compression-related electromagnetic ion cyclotron wave growth

J. P. McCollough,[1] S. R. Elkington,[2] and D. N. Baker[2]

[1] Electromagnetic ion cyclotron waves at high L values near local noon are often found to be related to magnetospheric compression events. These waves arise from temperature anisotropies in trapped warm plasma populations. There are several possible mechanisms that can generate these temperature anisotropies, including both energizing and nonenergizing processes. In this work we investigate a nonenergizing process arising from dayside bifurcated magnetic field minima. There are two kinds of behavior particles undergo in the presence of bifurcated minima: particles with high initial equatorial pitch angles (EPAs) are forced to execute so-called Shabansky orbits and mirror at high latitudes without passing through the equator, while those with lower initial EPAs will pass through the equator with higher EPAs than before; as a result, perpendicular energies near the equator increase at the cost of parallel energies. By using a 3-D particle tracing code in a tunable analytic compressed-dipole field, we explore the effects of Shabansky orbits on the anisotropy of the warm plasma and contrast with the anisotropy resulting from drift shell splitting. We show that Shabansky orbits are an independent source of temperature anisotropy for warm dayside ions.

## 1. Introduction

[2] *McCollough et al.* [2009] used an MHD/particle method to simulate the compression event of 29 June 2007. During this event, compression-related electromagnetic ion cyclotron (EMIC) waves were observed on the dayside using ground-based instruments and measurements by the THEMIS spacecraft [*Usanova et al.*, 2008]. The results agreed with observations and showed the pivotal role the cold plasma population has in EMIC wave growth. In addition, through calculation of the time evolution of the ion temperature, the temperature anisotropy that provided free energy for EMIC waves was shown to be due in part to nonenergizing processes. Finally, simulations by *McCollough et al.* [2010] showed strong anisotropy peaking off the equator, following a bifurcated $B_{min}$-plane. These results suggested some combination of drift shell splitting and the bulk execution of so-called Shabansky orbits [*Shabansky*, 1971] as the responsible mechanism for warm (keV) plasma temperature anisotropy critical for EMIC wave growth.

[3] Shabansky orbits have been studied previously in the context of trapped energetic particle dynamics [e.g., *Antonova and Shabansky*, 1968; *Shao et al.*, 2005; *Öztürk and Wolf*, 2007] as well as cusp dynamics [e.g., *Delcourt et al.*, 1992; *Antonova*, 1996; *Sheldon et al.*, 1998; *Delcourt and Sauvaud*, 1998, 1999] but not in the context of warm plasma temperature anisotropy generation. Particles undergo Shabansky orbits in response to bifurcation of the $B_{min}$-plane on the dayside of a compressed magnetosphere. This bifurcation leads to off-equatorial dayside drift motion at high latitudes. *Tsurutani and Smith* [1977] proposed the resulting off-equatorial "pockets" of minimum field strength could be source regions of high-latitude chorus waves, and observations of *Santolik et al.* [2010] support this idea. Here, an examination of the effects that bulk execution of these orbits has on warm ion temperature anisotropy in the absence of other possible mechanisms is presented.

[4] In order to study these effects in a controlled fashion, we use an analytic compressed dipole field introduced by *Kabin et al.* [2007]. By performing test particle simulations in a static magnetic field with no electric field, we can study the properties of a particle population in a bifurcated magnetic field configuration in an energization-free setting.

[5] After an introduction to the analytic model and a discussion of drift shell splitting (DSS) as a source of anisotropy, we show that anisotropy is present with and without the DSS source. We then examine trajectories of particles with different initial equatorial pitch angles $\alpha_0$ to show how a Shabansky field configuration leads to warm ion temperature anisotropy.

### 1.1. Analytic Stretched Dipole Field

[6] Building off of the equatorial compressed dipole field of *Elkington et al.* [2003], *Kabin et al.* [2007] introduced a

---

[1]Space Vehicles Directorate, Air Force Research Laboratory, Kirtland Air Force Base, New Mexico, USA.
[2]Laboratory for Atmospheric and Space Physics, University of Colorado at Boulder, Boulder, Colorado, USA.
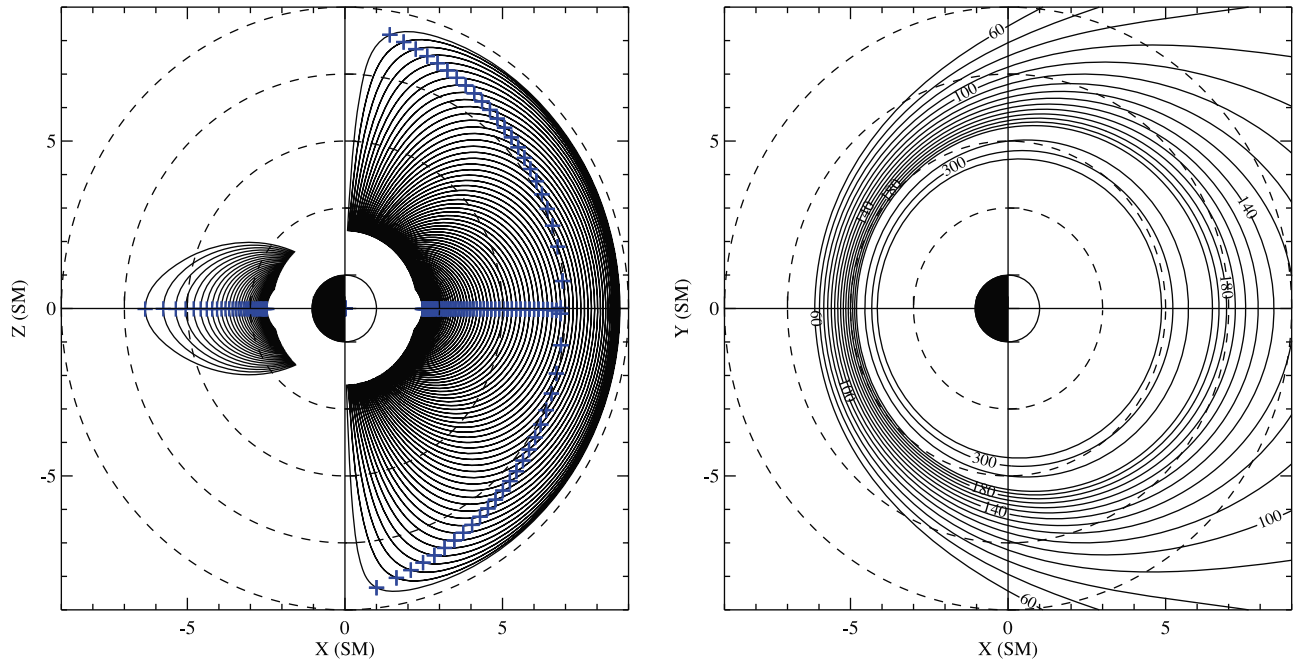
**Figure 1.** (left) Closed magnetic field lines in the noon-midnight plane and (right) magnetic field strength at the magnetic equator from equation (5). The blue crosses denote field-aligned magnetic minima. Parameters were $B_0 = 30000$ nT, $b_1 = 10$ nT, $b_2 = 8$. The dashed lines are concentric with Earth at 3, 5, 7, and 9 $R_E$.

three-dimensional analytic compressed dipole field for studying standing ULF waves in nonaxisymmetric magnetic fields. In terms of Euler potentials, this field can be written:

$$\vec{A} = \alpha \vec{\nabla} \beta, \tag{1}$$

$$\vec{B} = \vec{\nabla}\alpha \times \vec{\nabla}\beta, \tag{2}$$

$$\alpha = \frac{B_0}{r}\sin^2\theta - \frac{1}{m}r^2 b_1(1 + b_2\cos\phi)\sin^m\theta, \tag{3}$$

$$\beta = \phi. \tag{4}$$

Euler potentials have the advantage of providing the vector potential $\rightarrow A$, so induced electric fields can be calculated (if any of the parameters are time-dependent), and a straightforward means of determining field lines [*Stern*, 1966]. The parameter $m$ can take on any value greater than 2, but we follow *Kabin et al.* [2007] and choose $m = 2$. This simplifies the algebra and provides a realistic-looking field. Thus we have the following expression for the magnetic field:

$$\vec{B} = \hat{r}\left[\frac{2B_0}{r^3} - b_1(1 + b_2\cos\phi)\right]\cos\theta$$
$$+ \hat{\theta}\left[\frac{B_0}{r^3} + b_1(1 + b_2\cos\phi)\right]\sin\theta, \tag{5}$$

where $B_0$ is the magnetic field strength on the Earth's surface at the equator, $b_1$ is analogous to IMF strength (and has units of magnetic field strength), and $b_2$ is a dimensionless

parameter that acts similar to solar wind dynamic pressure by compressing the field. Equation (5) uses a geocentric spherical coordinate system with units of length in Earth radii. It is clear that setting $b_1 = 0$ reduces equation (5) to a dipole magnetic field. This field does not include dipole tilt, restricting bifurcation to be symmetric in both hemispheres (unlike the bifurcated MHD fields of *McCollough et al.* [2010]).

[7] Figure 1 shows closed magnetic field lines in the noon-midnight plane (left) and magnetic field strength at the magnetic equator (right) from equation (5) with $B_0 = 30000$ nT, $b_1 = 10$ nT, $b_2 = 8$. The blue crosses denote field-aligned magnetic minima $B_{\min}$. It is easy to see that the $B_{\min}$-plane bifurcates near a radial distance of 7 $R_E$ in the noon sector. For this study, we have fixed $B_0$ and $b_1$ to the values used for Figure 1 and varied $b_2$.

[8] The T96 empirical field model [*Tsyganenko*, 1995, 1996] exhibits similar bifurcation for compressed configurations. It is not used in this study because it does not give reliable results for the regions near the magnetopause where these bifurcations occur. This is not an issue for the analytic field since there is no magnetopause in the sense of a physical current-defined boundary.

## 1.2. Model Parameters Versus Realistic Models

[9] To provide a connection between $b_2$ and the MHD fields used by *McCollough et al.* [2009] and *McCollough et al.* [2010], we examine the ratio of magnetic field strength at $r_0 = 6$ $R_E$ along the magnetic equator at two local times: noon and dusk. We choose this ratio because it is a proxy for the amount of compression that can easily be compared to other models and observations. We use dusk

instead of midnight to avoid the effects of reconnection and dipolarization in the tail. For our analytic field, this ratio can be written as

$$\rho_B = 1 + \frac{b_1 b_2}{B_0/r_0^3 + b_1}. \tag{6}$$

For this study, this reduces to $\rho_B = 1 + 0.0672 b_2$. For comparison, the values of $\rho_B$ from the MHD fields of *McCollough et al.* [2009] before the compression event of 29 June 2007 and during the event are $\rho_B = 1.135$ and $\rho_B = 1.196$, respectively. Values from T96 for the same periods are $\rho_B = 1.125$ and $\rho_B = 1.195$. The postcompression values suggests that a value of 3 for $b_2$ would provide a similar geometry to the geomagnetic field during the compression event.

[10] For a more extreme case, a compression event observed by GOES-8 and GOES-9 on 6 November 1997 had a value of 1.756 for $\rho_B$, which corresponds to a $b_2$ value of 11.25. This compression event was not unusual, and many events have been catalogued with similar $\rho_B$ values [*Turner et al.*, 2010].

### 1.3. Drift Shell Splitting as Anisotropy Generation Mechanism

[11] When particles drift around the Earth, conservation of the first and second adiabatic invariants $\mu$ and $J$ means that particles with high initial equatorial pitch angles $\alpha_{eq}^0$ end up on drift paths further out in $L^*$ on the dayside than those with lower $\alpha_{eq}^0$, a phenomenon known as "drift shell splitting" [*Roederer*, 1967]. When the omnidirectional differential particle flux decreases as a function of $L^*$, an excess of near-equatorial particles relative to lower $\alpha_{eq}^0$ populations appears at higher $L^*$ values [e.g., *Kaufmann*, 1987]. This creates an excess of perpendicular energy, and a temperature anisotropy $A = T_\perp/T_\parallel - 1$ emerges.

[12] In contrast, if the flux is constant in $L^*$, every near-equatorial particle moving to a higher $L^*$ value is simply replacing one that is now further out, so the overall anisotropy would not increase. Anisotropy emerging from DSS can thus be "turned off" by replacing a realistic flux (such as AP-8 [see *McCollough et al.*, 2009]) with one that is constant as a function of $L^*$.

[13] In this work, using the fields of *Kabin et al.* [2007], we define a proxy for $L^*$ in the following way:

$$L = \left(\frac{B_0}{B_i}\right)^{1/3}. \tag{7}$$

Here, $B_0$ is the dipole field strength at the Earth's surface for the analytic fields, and $B_i$ is the magnetic field at the equatorial crossing of the given particle. This can be justified by recalling that the drift path for particles with $\alpha_{eq}^0 = 90°$ follow lines of constant magnetic field strength, and this is approximately true for particles with lower $\alpha_{eq}^0$. This provides an $L$ value similar in spirit to $L^*$, but without having to compute the magnetic flux required for $L^*$ [see *Roederer*, 1970].

[14] Energetic particle studies [*Gannon et al.*, 2007] have shown that pitch angle distributions are mostly pancake (indicating a positive temperature anisotropy parameter $A$) or flattop (isotropic) during quiet periods, with butterfly distributions confined to near midnight and disturbed conditions. Butterfly distributions are associated with negative anisotropies but are relatively rare. Thus DSS-induced effects will raise the anisotropy and yield a significant positive anisotropy most of the time.

## 2. Anisotropy Generation in the Absence of a Decreasing Radial Flux Profile

[15] We performed test particle simulations in the magnetic field of equation (5) for a set of $b_2$ values, ranging from 0 to 10. This range was chosen to cover the range of configurations from pure dipole to large compression events. For this study, we are only interested in anisotropy generation. We chose to simulate hydrogen ions as they make up the bulk of the warm plasma population. The energy range was the same as used by *McCollough et al.* [2009], 20 keV $\leq KE \leq$ 300 keV, and the maximum radial distance was expanded from 8 to 9 $R_E$. The minimum radial distance was kept at 3 $R_E$ and the particles are launched from the equatorial plane randomly within 10s of simulation start. Each simulation consisted of calculating trajectories for 8 million particles launched isotropically in this region over the course of 1 simulated hour.

[16] Figures 2–4 show the temperature anisotropy $A$ in the SM X-Z plane for $b_2 = 1$, $b_2 = 3$, and $b_2 = 8$, respectively, after 50 min of simulation time. This allows for the bulk of the particles to have executed most of a complete drift period. Shown on the left is the anisotropy with a constant flux in $L$ and on the right is the anisotropy using the AP-8 flux. The anisotropy is only plotted in regions of closed magnetic field lines, since we are only interested in the trapped particle dynamics. The local field-aligned minima are denoted by blue crosses.

[17] Figure 2 shows anisotropy arising from a slightly compressed ($b_2 = 1$) field. Bifurcation of the $B_{min}$ plane occurs but does so outside the region our particle population inhabits (bifurcated minima can be seen at the extreme sunward corners). It is easy to see in this case that with a constant flux, the only anisotropy that exists is that due to the bounce loss cone arising from a lack of isotropizing processes at lower values of $L$. In contrast, using AP-8, a flux model that decreases with $L$, produces anisotropy that peaks at high values of $L$, and at lower latitudes. This is consistent with what we would expect from DSS-induced anisotropy. Thus using a constant flux does isolate anisotropy calculations from the DSS source.

[18] Figure 3 shows anisotropy arising from a field with significant compression ($b_2 = 3$), comparable to the MHD field of *McCollough et al.* [2009]. There is bounce-loss anisotropy, as before, but there is now significant anisotropy off the equator and in the vicinity of the bifurcated $B_{min}$ plane, even with a flux constant in $L$. This enhanced anisotropy is confined to a field-aligned region for field lines with off-equatorial minima. Because the anisotropy appears even with the DSS source "turned off," the anisotropy arises from the Shabansky magnetic field configuration alone and is clearly a separate effect from DSS-induced anisotropy.

[19] Figure 4 shows the anisotropy in a very compressed ($b_2 = 8$) field. Figure 4 has similar features to Figure 3:
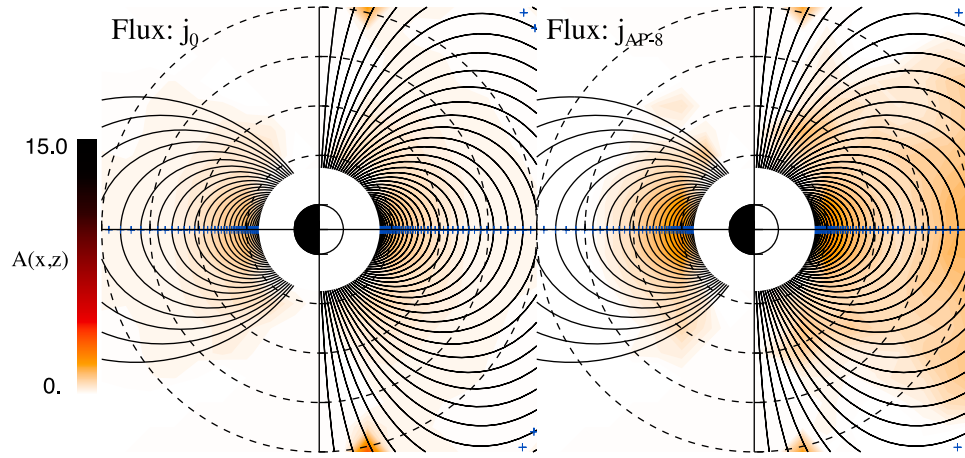
**Figure 2.** Hydrogen anisotropy in the SM X-Z plane for a $b_2$ value of 1.0, with (left) a flux constant in $L$ and (right) the AP-8 flux after 50 min of simulation time. The anisotropy is only plotted in regions of closed magnetic field lines, since we are only interested in the trapped particle dynamics. The local field-aligned minima are denoted by blue crosses. In this case with a constant flux, the only anisotropy that exists is that due to the bounce loss cone arising from a lack of isotropizing processes at lower values of $L$. In contrast, using AP-8, a flux model that decreases with $L$, produces anisotropy that peaks at high values of $R$, and at lower latitudes which is consistent with DSS-induced anisotropy.

bounce-loss anisotropy at lower $L$-values, and a region of high anisotropy along field lines with bifurcation of the $B_{min}$ plane. Since we are interested specifically in this Shabansky mechanism, we will look at particle trajectories in this very distorted field to determine clues as to how this field configuration produces anisotropies on the dayside, both off the equator and near the equator.

[20] It should be noted that the anisotropies plotted in Figures 2–4 do not include the effects EMIC waves will have in reducing the anisotropy [*Gary et al.*, 1994]. When EMIC waves are amplified, they reduce the anisotropy until marginal stability is obtained at a specific anisotropy value [*Anderson and Fuselier*, 1994]. Therefore the anisotropies plotted here should be considered peak values that would

diminish as EMIC waves are amplified. Observation-based studies [*Blum et al.*, 2009] use this criterion to infer EMIC wave growth in a complementary approach to the one used by *McCollough et al.* [2009].

## 3. Anisotropy Arising From Magnetic Field Configuration

[21] *McCollough et al.* [2010] suggested a means for temperature anisotropy to develop in response to a bifurcated $B_{min}$ plane that assumed qualitatively different particle behaviors for particles of different initial equatorial pitch angle. This is supported by the densities plotted in Figure 5: the density on the left is for lower initial equatorial pitch
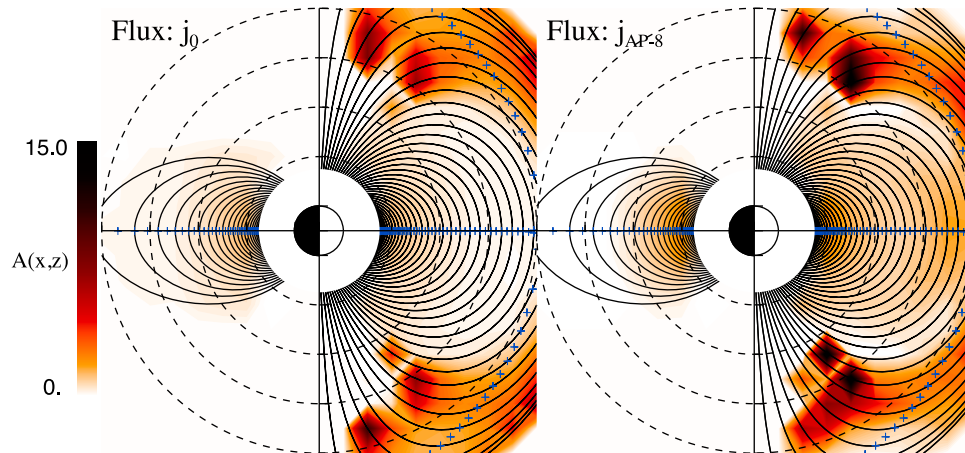


**Figure 3.** Hydrogen anisotropy in the SM X-Z plane for a $b_2$ value of 3.0, with (left) a flux constant in $L$ and (right) the AP-8 flux in the same manner as Figure 2. This field has a $b_2$ value comparable to the MHD field of *McCollough et al.* [2009]. There is bounce-loss anisotropy, as before, but there is now significant anisotropy off the equator and in the vicinity of the bifurcated $B_{min}$-plane, even with a flux constant in $L$.
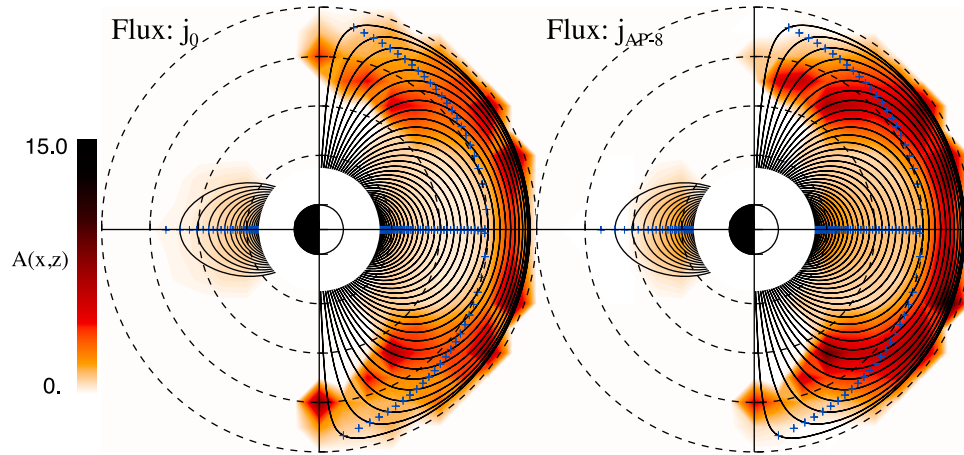
**Figure 4.** Hydrogen anisotropy in the SM X-Z plane for a $b_2$ value of 8.0, with (left) a flux constant in $L$ and (right) the AP-8 flux in the same manner as Figure 2. Features are similar to Figure 3: bounce-loss anisotropy at lower $L$-values, and a region of field-aligned high anisotropy determined by bifurcation of the $B_{min}$ plane.

angles ($\alpha_{eq}^0 < 30°$), and is almost exclusively confined to small radial distances where the field minima do not bifurcate (i.e., there is one minimum along a field line), while the density on the right ($\alpha_{eq}^0 > 60°$) extends along the bifurcated $B_{min}$-plane to higher latitudes.

[22] In Figure 6 we have plotted contours of constant magnetic field strength for $b_2 = 3$ and $b_2 = 8$. Equatorially mirroring particles will drift along these contours if the first adiabatic invariant is conserved. The thick red line corresponds to the point at which the $B_{min}$ plane bifurcates and branches away from the magnetic equator. We will use the term "Shabansky region" to define the spread in MLT of this region. For Figure 6 it is clear that the Shabansky region for $b_2 = 3$ and a maximum radius of $R = 9$ is 08:00–16:00 MLT and the region for $b_2 = 8$ is approximately 07:00–17:00 MLT.

[23] With the analytic field, we followed test particles with different initial equatorial pitch angles and computed several quantities of interest: the kinetic energy $KE$ of the particle, the first adiabatic invariant $\mu$, the field-geometric integral

$I = J/2p$ (with $J$ the second invariant and $p$ the mechanical momentum), and the magnetic field along the guiding-center field line. On the basis of these studies, we separated the particles into four types, according to the characteristics of their trajectories. Each type and its role in the resulting temperature anisotropy is described below, in the context of sample trajectories of particles launched from the same nightside location ($R_0 = 5.5$, $\phi_0 = 150°$) with different pitch angles.

## 3.1. Non-Shabansky Particles

[24] Non-Shabansky particles execute dayside drifts without passing through the bifurcated region of the magnetic field. A non-Shabansky particle trajectory in a $b_2 = 8$ field is displayed along with $I$ in Figure 7. The first invariant $\mu = 31$ MeV/G is conserved within 10% and the kinetic energy $KE = 200$ keV is conserved within 0.02%. Thus $I$, $\mu$, and $KE$ are all conserved for this particle throughout the simulation. The drift-periodic "fuzziness" in $I$ and $\mu$ is due
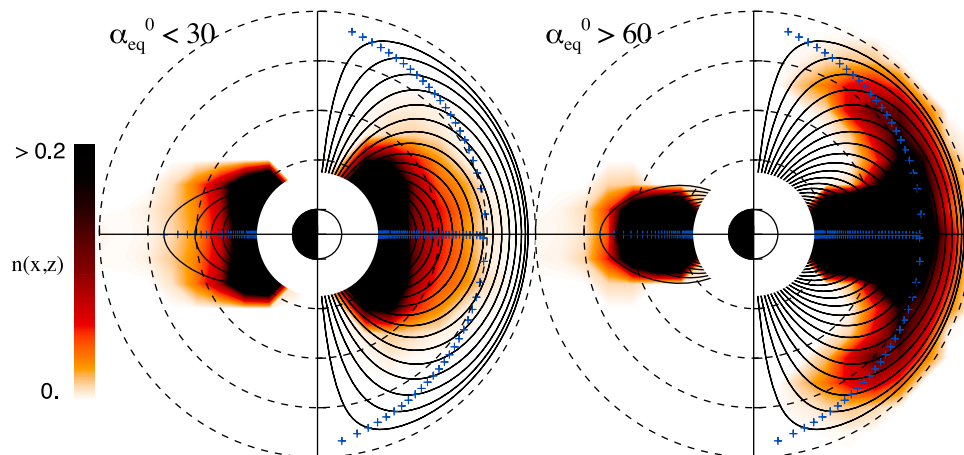


**Figure 5.** Hydrogen densities in the SM X-Z plane for a $b_2$ value of 8, for particles with (left) $\alpha_0 < 30°$ and (right) $\alpha_0 > 60°$. These number densities are in units of /cc. As previously indicated, 50 min of simulation time have elapsed.
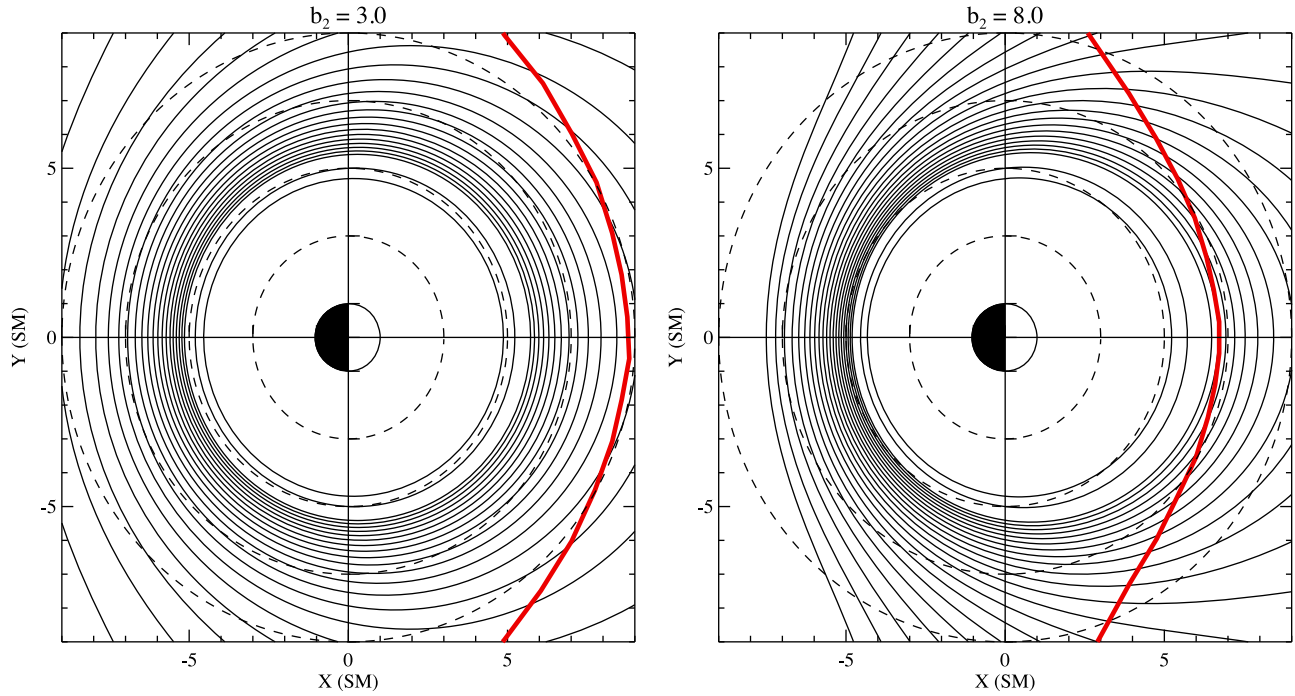
**Figure 6.** Contours of magnetic field strength for $b_2 = 3$ and $b_2 = 8$. The red line indicates the boundary between regions of bifurcated and nonbifurcated magnetic minima.

to strong magnetic field curvature near midnight [*Young et al.*, 2002], and the small-amplitude higher-frequency fluctuations are due to numerical errors in calculating $\mu$. The only way these particles contribute to anisotropy is through DSS-induced anisotropy, since their motion is adiabatic. This is due to the particle drifting without passing through the bifurcated fields.

[25] Figure 7 shows the magnetic field profile just outside (Figure 7, left) and just inside (Figure 7, right) the Shabansky region. The mirror field strength,

$$B_m = \frac{p^2}{2m_0\mu} = \frac{KE}{\mu} \qquad (8)$$

is indicated by the dashed line. The last expression is only accurate for nonrelativistic energies, which is an appropriate approximation for the populations used here. Recalling the expression for the mirror force [*Northrop*, 1963]:

$$\vec{F}_{\mathrm{mirror}} = -\frac{\mu}{\gamma}\left(\hat{B} \cdot \vec{\nabla}\right)B = -\frac{\mu}{\gamma}\nabla_\parallel B, \qquad (9)$$

it is obvious that the field strength along a field line $B(s)$ functions as a potential, so in the lower portion of Figure 7, a particle will move along the field line up to $B_m$, where the particle slows to a stop and turns around, as in a graviational well. It is clear from this that particle motion in the Shabansky region is unchanged in the adiabatic sense from motion outside the region, since there is only one minimum and it is at the equator.

### 3.2. Shabansky I Particles

[26] Shabansky I particles pass through both hemispheres along field lines with bifurcated minima in the Shabansky

region. A Shabansky I particle trajectory is shown in Figure 8. The first invariant $\mu = 125$ MeV/G is conserved within 10% and the kinetic energy $KE = 200$ keV is conserved within 0.02%. Thus like the non-Shabansky particle, this particle also conserves $I$, $\mu$, and $KE$. $I$ has some short dips in the Shabansky region (between times $t = 20$ min and $t = 30$ min) that correspond to numerical limitations of computing $I$. These artifacts are due to the fact that the mirror field strength for this particle is only slightly greater than the field strength at the equator. The small bounce-frequency error in $\mu$ mentioned in section 3.1 is reflected in the $B_m$ value. Near the equator this $B_m$ can fall very close or even below the total field strength, which leads to an incorrect value for $I$ near zero. It is apparent, aside from this numerical artifact, that $I$ is conserved throughout the simulation period.

[27] Although $I$, $\mu$, and $KE$ are conserved, these particles contribute to the temperature anisotropy near the equator, which can be understood by considering the following. Figure 8 (bottom) shows the magnetic field profile for a Shabansky I particle in the same manner as Figure 7. Inside the Shabansky region, there is a "hump" near the equator where magnetic field increases along the field line. As a particle bounces along this field line near the equator, it transfers parallel energy into perpendicular energy in order to conserve $\mu$ and $KE$, since the magnetic field increases to a local maximum at the equator. All Shabansky I particles must do this, and the result is a net increase in perpendicular temperature at the cost of parallel temperature. Thus a temperature anisotropy arises near the equator in the Shabansky region. In addition, since these particles are conserving $\mu$ and $I$, they will contribute to DSS-induced anisotropy.
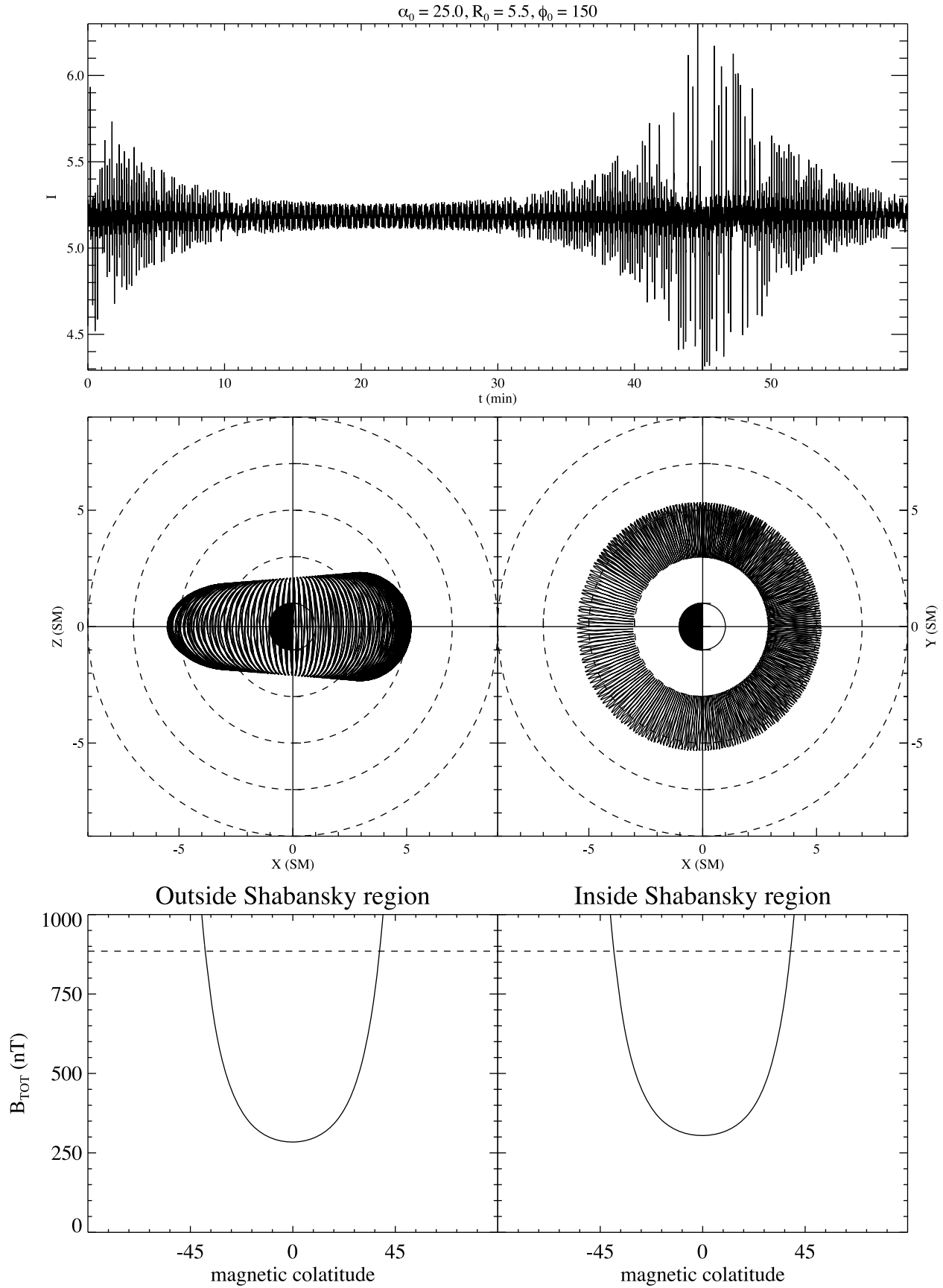
**Figure 7.** *I*, trajectory projections, and magnetic field profiles for a non-Shabansky particle. The mirror field is indicated by the dashed line in the field profile.

**Figure 8.** *I*, trajectory projections, and magnetic field profiles for a Shabansky *I* particle. The mirror field is indicated by the dashed line in the field profile.
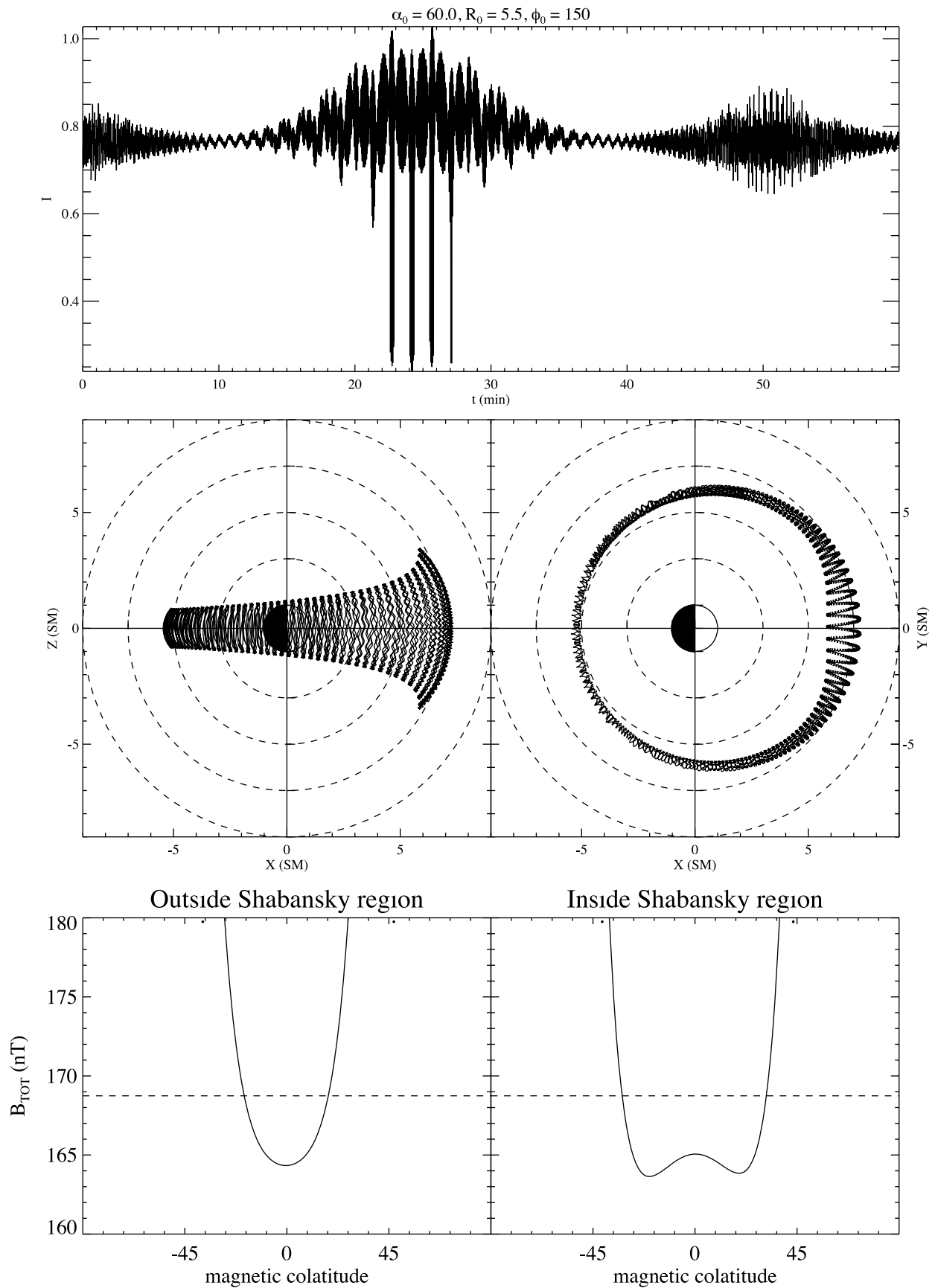
### 3.3.  Shabansky II Particles

[28] Shabansky II particles execute "classic" Shabansky orbits, spending most of their time in the Shabansky region at high latitudes in one hemisphere. Figure 9 displays a Shabansky II trajectory. The first invariant $\mu = 155$ MeV/G is conserved within 10% and the kinetic energy $KE = 200$ keV is conserved within 0.02%. A key feature of Shabansky II orbits is the breaking of the second adiabatic invariant, evidenced by the sudden change in value of $I$ as the particle enters (near $t = 13$ min) and leaves ($t = 28$ min) the Shabansky region. This shift to a lower value of $I$, and thus $J$, indicates a loss of parallel momentum (since $J = \oint p_\parallel ds$) during the off-equatorial portion of the particle trajectory; since $KE$ is conserved, this implies a shift in energy from the parallel component to the perpendicular component.

[29] The loss of $p_\parallel$ can be thought of in another way: since $\mu$ and $KE$ are conserved and these ions are at nonrelativistic energies, $B_m$ is constant (see equation (8)). Figure 9 shows that as the particle moves into the Shabansky region, it is forced into a region with higher $B_{\min}$ than before. This results in a higher minimum pitch angle and thus more perpendicular energy at the cost of parallel energy.

[30] *Shao et al.* [2005] studied the time-evolution of $J$ for warm protons in LFM-generated electromagnetic fields and saw similar features. In addition, we have noticed that these Shabansky II particles tend to have approximately the same $I$ value after leaving the Shabansky region as before entering, which is different from Shabansky III particles. This "conservation" of $I$ in a drift sense was also noted by *Shao et al.* [2005].

[31] The breaking of the second invariant can be seen clearly in Figure 9 (bottom). Outside the Shabansky region, the particle mirrors in a "single well". Inside, it finds itself stuck in one of two wells, with the mirror field closer to the minimum field strength. This lowers $J$, which leads to a transfer of parallel energy to perpendicular energy and thus increased temperature anisotropy.

### 3.4.  Shabansky III Particles

[32] Shabansky III particles are initially near-equatorial ($\alpha_{eq}^0 \gtrsim 85°$) particles that undergo Shabansky orbits but do not enhance anisotropy. A Shabansky III trajectory is shown in Figure 10. The first invariant $\mu = 157$ MeV/G is conserved within 10% and the kinetic energy $KE = 200$ keV is conserved within 0.02%. The key difference between type III and type II particles is what happens to $I$ as the particle enters the Shabansky region. While a type II particle lowers $I$ as it enters the Shabansky region, these near-equatorial particles have such small initial $I$ values that $I$ is no longer lowered but is broken and can increase in value or stay close to the same value as before. This change in behavior can be thought of as a result of a "zero bound problem": $I$ cannot be negative. *Öztürk and Wolf* [2007] discussed this distinction between "equatorial" and "nonequatorial" particles, corresponding to types III and II, respectively.

[33] The difference between types III and II is evident in Figure 10. Similar to type II particles (Figure 9), these particles find themselves trapped in one well inside the Shabansky region. In this case, $B_{\min}$ is lowered, so they can have parallel momentum (or $KE$) enhanced.

[34] Breaking $I$ leads to breaking the third adiabatic invariant which keeps $\mu$ and $KE$ fixed. Evidence of this is seen in the SM X-Y projection of the trajectory in Figure 10. One can see on the second orbit that the guiding center on the nightside is further out in radius. This is an explanation for why $B_{\min}$ is raised for type II particles and lowered for type III particles: To keep $\mu$ fixed, type II particles must move inward in $L^*$, corresponding to stronger fields, and type III particles must move outward in $L^*$, corresponding to weaker fields. By increasing their $I$ value significantly in the Shabansky region, type III particles can decrease the anisotropy there.

[35] The lack of "conserving" $I$ in the sense of section 3.3 appears to be a diffusive process. By breaking $I$, the particles must break the third invariant as well; in an asymmetric field this will lead to radial diffusion. Diffusion in phase space is an important component in the dynamics of energetic particles in the magnetosphere and can be responsible for energization and loss (see *Schulz and Lanzerotti* [1974] for a detailed treatment). The implications and study of this potentially new diffusive process is the subject of future research.

### 3.5.  Features of Anisotropy Profiles

[36] To summarize the different particle behaviors, we have the following types:

[37] 1. Non-Shabansky particles execute dayside drifts without passing through the bifurcated region of the magnetic field. They conserve $\mu$, $I$, and $KE$ throughout an orbit.

[38] 2. Shabansky I particles pass through both hemispheres in the presence of a bifurcated field. They also conserve $\mu$, $I$, and $KE$ throughout an orbit.

[39] 3. Shabansky II particles stay in one hemisphere while drifting through the bifurcation. They conserve $\mu$ and $KE$. $I$ is lower while in the Shabansky region than during the rest of the drift motion. The value of $I$ returns to its approximate initial value upon exiting the Shabansky region.

[40] 4. Shabansky III particles also stay in one hemisphere while drifting through the bifurcation but have an increased $I$ while in the Shabansky region. They do not recover the initial $I$ value after executing a complete orbit.

[41] A key discriminator between different Shabansky types is the initial value of $I$: type I have the largest $I$ (corresponding to lower values of $\alpha_{eq}^0$), type II have smaller values, and type III have near-zero values. We can thus make the correspondence between low, high, and near-equatorial $\alpha_{eq}^0$ with Shabansky I, II, and III, respectively.

[42] With both Shabansky II and III particles present, it is prudent to ask if the net effect is an increase in anisotropy. The answer comes from the amount of type III particles relative to type II particles: with an initially isotropic distribution, the number of particles is constant for different values of $\alpha_{eq}^0$. The number of particles that would undergo type II particle motions is significantly larger than the near-equatorial range required for type III behavior, so the total anisotropy increases in these off-equatorial regions.

[43] Looking back at the left-hand sides of Figures 2–4, we can begin to understand how the anisotropy arises. We can see the anisotropy due to the lack of isotropizing process in the inner nonbifurcated region, getting weaker at further radial distances. In addition, Figures 3 and 4 show anisotropy in the bifurcated region and at high latitudes for
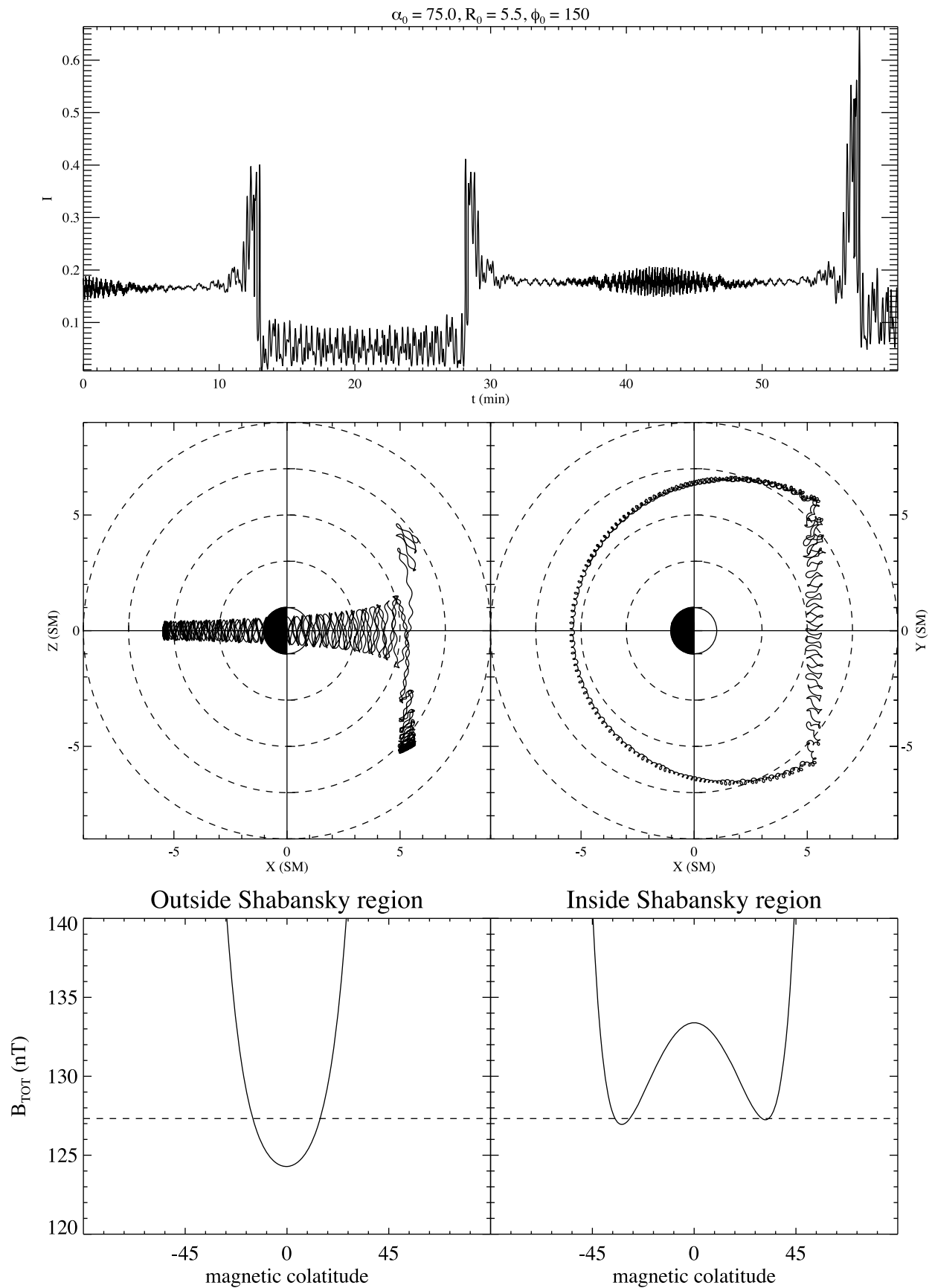
**Figure 9.** *I*, trajectory projections, and magnetic field profiles for a Shabansky II particle. The mirror field is indicated by the dashed line in the field profile.

**Figure 10.** *I*, trajectory projections, and magnetic field profiles for a Shabansky III particle. The mirror field is indicated by the dashed line in the field profile.
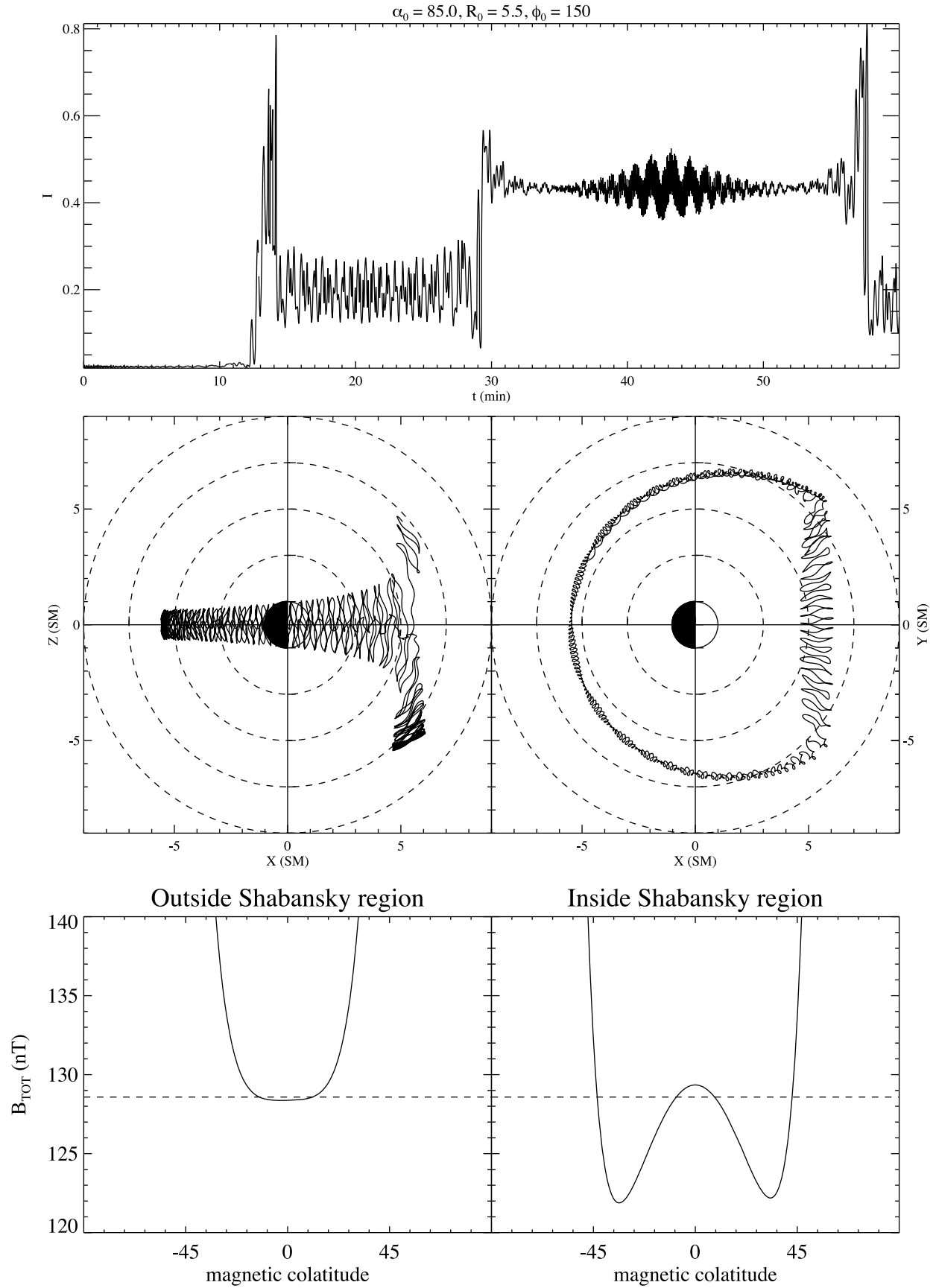
bifurcated field lines due to Shabansky II particles. Figure 4 shows anisotropy near the equator in the bifurcated region from Shabansky I "hump"-induced anisotropy. This is happening for $b_2 = 3$, but is off the plotting area of Figure 3.

[44] The right-hand side, with DSS-induced anisotropy "switched on" using AP-8 instead of a flat flux profile, enhances the anisotropy in a straightforward manner. For the $b_2 = 1$ case (Figure 2), almost all the anisotropy at higher radial distances is DSS-induced and is centered at the equator as one would expect. In Figures 3 and 4, it is easy to see the DSS-induced anisotropy enhances the total anisotropy at all radial distances near the equator, but the anisotropy seems to decrease slightly at very high latitudes along the bifurcated $B_{min}$-plane. This is likely due to DSS occurring outside the Shabansky region, which is most significant for particles with the highest pitch angles and the largest drift radii. Because of this, the particles that find themselves at the highest latitudes in the XZ-plane are disproportionately Shabansky III particles which do not increase the anisotropy.

## 4. Discussion

[45] A magnetic field configuration with off-equatorial dayside minima separates the particles into four types, discriminated by initial equatorial pitch angle. The different regions in latitude and $L$ traversed by the different types suggests a new source of warm ion anisotropy generation and thus EMIC wave growth.

[46] Since warm temperature anisotropy is the driver of EMIC wave growth, this is a new potential source free energy for EMIC wave growth [*Kozyra et al.*, 1984; *McCollough et al.*, 2010]. The effect is truly three-dimensional: other magnetospheric models where EMIC wave growth rates have been calculated [e.g., *Jordanova et al.*, 2008; *Gamayunov et al.*, 2009] have used bounce-averaged equations and thus cannot see the violation of $I$ we have documented here.

[47] We assumed a static geomagnetic field and no geoelectric field to isolate nonenergizing mechanisms. Relaxing these would presumably augment the DSS and Shabansky anisotropy sources with the induced electric field source of *Olson and Lee* [1983] and shock-induced and radial transport discussed by *Summers et al.* [1998].

[48] *McCollough et al.* [2009] and *McCollough et al.* [2010] looked at anisotropy development and wave growth rates in the magnetic equator based on the assumption that this is where wave generation peaked in latitude. The bifurcated magnetic field configurations studied here and seen in Figure 10 of *McCollough et al.* [2010], however, suggest that off-equatorial EMIC wave generation in response to magnetic compression may be important. The anisotropy can become significantly higher off the equator, leaving more free energy to be dissipated as EMIC waves. In addition, since the field is weaker off the equator, and wave growth has an inverse relationship with the Alfvén speed, waves should be generated more often near the field minima than near the equator.

[49] The analytic field used in this study is different from more realistic field models. The dayside region of Figure 1 can be contrasted with Figure 10 of *McCollough et al.* [2010]. There is no north–south asymmetry, and the bifurcation line takes a different shape. Additionally, at higher

$L$ shells, the presence of the magnetopause and boundary layer would have significant effects on particle dynamics. However, bifurcation itself is exhibited in both, and the effect of this feature on trapped particles is what we focused on in this study.

[50] As discussed by *McCollough et al.* [2010], a cold background plasma population is required for the free energy available from the warm anisotropy to be transformed into EMIC wave energy. In the magnetosphere, this is provided by the plasmasphere. At high $L$ shells where these off-equatorial minima occur, it is possible that plasmaspheric plumes or other features could play this role. Further research of the conditions under which this occurs is crucial to understanding the connection between Shabansky orbits and EMIC wave generation.

[51] Unlike convection-driven EMIC waves [*Summers et al.*, 1998], where electric fields produce anisotropies in newly convected plasma sheet ions, it is not obvious how the origin of Shabansky-driven anisotropy (the bifurcated $B_{min}$ plane) is quenched by EMIC waves. How Shabansky orbits are subsequently affected by the growth of EMIC waves in the Shabansky region is not clear and the subject of our current research.

[52] The pitch angle boundaries separating the Shabansky types depend on many parameters, including drift shell, magnetic field parameters $b_1$ and $b_2$, drift phase, bounce phase, and possibly even gyrophase [*Young et al.*, 2002]. Shabanksy Orbit Accessibility Maps (SOAMs) calculated by *Shao et al.* [2005] show the critical role initial equatorial pitch angle and launch location have on behavior in the Shabansky region. These SOAMs show significant fine structure, blurring the particle type boundaries in pitch angle and location. The results here are consistent with this and show the effects on temperature anisotropy.

## 5. Conclusion

[53] We explored a new means of anisotropy generation in warm ions arising from global geomagnetic field configuration. We have shown that Shabansky orbits executed in bulk provide a temperature anisotropy distinct from DSS-induced temperature anisotropy. This new physical mechanism for anisotropy generation has two origins: the breaking of the second adiabatic invariant by Shabansky II particles and the conversion of parallel energy to perpendicular energy as Shabansky I particles pass through the equator.

## References

Anderson, B. J., and S. A. Fuselier (1994), Response of thermal ions to electromagnetic ion cyclotron waves, *J. Geophys. Res.*, 99, 19,413–19,425.

Antonova, A. E. (1996), High-latitude particle traps and related phenomena, *Radiat. Meas.*, 26(3), 409–411.

Antonova, A. E., and V. P. Shabansky (1968), Structure of the geomagnetic field at great distance from the Earth, *Geomagn. Aeron.*, 8, 801–811.

Blum, L. W., E. A. MacDonald, S. P. Gary, M. F. Thomsen, and H. E. Spence (2009), Ion observations from geosynchronous orbit as a proxy

for ion cyclotron wave growth during storm times, *J. Geophys. Res.*, *114*, A10214, doi:10.1029/2009JA014396.

Delcourt, D. C., and J. A. Sauvaud (1998), Recirculation of plasma sheet particles into the high-latitude boundary layer, *J. Geophys. Res.*, *103*, 26,521–26,532.

Delcourt, D. C., and J. A. Sauvaud (1999), Population of cusp and boundary layers by energetic (hundreds of keV) equatorial particles, *J. Geophys. Res.*, *104*, 22,635–22,648.

Delcourt, D. C., T. E. Moore, J. A. Sauvaud, and C. R. Chappell (1992), Nonadiabatic transport features in the outer cusp region, *J. Geophys. Res.*, *97*, 16,833–16,842.

Elkington, S. R., M. K. Hudson, and A. A. Chan (2003), Resonant acceleration and diffusion of outer zone electrons in an asymmetric geomagnetic field, *J. Geophys. Res.*, *108*(A3), 1116, doi:10.1029/2001JA009202.

Gamayunov, K. V., G. V. Khazanov, M. W. Liemohn, M.-C. Fok, and A. J. Ridley (2009), Self-consistent model of magnetospheric electric field, ring current, plasmasphere, and electromagnetic ion cyclotron waves: Initial results, *J. Geophys. Res.*, *114*, A03221, doi:10.1029/2008JA013597.

Gannon, J. L., X. Li, and D. Heynderickx (2007), Pitch angle distribution analysis of radiation belt electrons based on Combined Release and Radiation Effects Satellite Medium Electrons A data, *J. Geophys. Res.*, *112*, A05212, doi:10.1029/2005JA011565.

Gary, S. P., M. B. Moldwin, M. F. Thomsen, D. Winske, and D. J. McComas (1994), Hot proton anisotropies and cool proton temperatures in the outer magnetosphere, *J. Geophys. Res.*, *99*, 23,603–23,615.

Jordanova, V. K., J. Albert, and Y. Miyoshi (2008), Relativistic electron precipitation by EMIC waves from self-consistent global simulations, *J. Geophys. Res.*, *113*, A00A10, doi:10.1029/2008JA013239.

Kabin, K., R. Rankin, I. R. Mann, A. W. Degeling, and R. Marchand (2007), Polarization properties of field line resonances in non-axisymmetric background magnetic fields, *Ann. Geophys.*, *25*(3), 815–822.

Kaufmann, R. L. (1987), Substorm currents: Growth phase and onset, *J. Geophys. Res.*, *92*, 7471–7486.

Kozyra, J. U., T. E. Cravens, A. F. Nagy, E. G. Fontheim, and R. S. B. Ong (1984), Effects of energetic heavy ions on electromagnetic ion cyclotron wave generation in the plasmapause region, *J. Geophys. Res.*, *89*, 2217–2233.

McCollough, J. P., S. R. Elkington, and D. N. Baker (2009), Modeling EMIC wave growth during the compression event of 29 June 2007, *Geophys. Res. Lett.*, *36*, L18108, doi:10.1029/2009GL039985.

McCollough, J. P., S. R. Elkington, M. E. Usanova, I. R. Mann, D. N. Baker, and Z. C. Kale (2010), Physical mechanisms of compressional EMIC wave growth, *J. Geophys. Res.*, *115*, A10214, doi:10.1029/2010JA015393.

Northrop, T. G. (1963), *The Adiabatic Motion of Charged Particles*, Wiley-Interscience, New York.

Olson, J. V., and L. C. Lee (1983), Pc 1 wave generation by sudden impulses, *Planet. Space Sci.*, *31*(3), 295–302.

Öztürk, M. K., and R. A. Wolf (2007), Bifurcation of drift shells near the dayside magnetopause, *J. Geophys. Res.*, *112*, A07207, doi:10.1029/2006JA012102.

Roederer, J. G. (1967), On the adiabatic motion of energetic particles in a model magnetosphere, *J. Geophys. Res.*, *72*, 981–992.

Roederer, J. G. (1970), *Dynamics of Geomagnetically Trapped Radiation*, 166 pp., Springer, New York.

Santolik, O., J. S. Pickett, D. A. Gurnett, J. D. Menietti, B. T. Tsurutani, and O. Verkhoglyadova (2010), Survey of poynting flux of whistler mode chorus in the outer zone, *J. Geophys. Res.*, *115*, A00F13, doi:10.1029/2009JA014925.

Schulz, M., and L. J. Lanzerotti (1974), *Particle Diffusion in the Radiation Belts*, Physics Chem. Space, vol. 7, 215 pp., Springer, New York.

Shabansky, V. P. (1971), Some processes in the magnetosphere, *Space Sci. Rev.*, *12*(3), 299–418.

Shao, X., S. F. Fung, L. C. Tan, K. Papadopoulos, M. Wiltberger, and M. C. Fok (2005), Investigation of 3D energetic particle transport inside quiet-time magnetosphere using particle tracing in global MHD model, in *The Inner Magnetosphere: Physics and Modeling, Geophys. Monogr. Ser.*, vol. 155, edited by T. I. Pulkkinen, N. A. Tsyganenko, and R. H. Friedel, pp. 307–318, AGU, Washington, D. C., doi:10.1029/155GM33.

Sheldon, R. B., H. E. Spence, J. D. Sullivan, T. A. Fritz, and J. Chen (1998), The discovery of trapped energetic electrons in the outer cusp, *Geophys. Res. Lett.*, *25*, 1825–1828.

Stern, D. P. (1966), The motion of magnetic field lines, *Space Sci. Rev.*, *6*(2), 147–173.

Summers, D., R. M. Thorne, and F. L. Xiao (1998), Relativistic theory of wave-particle resonant diffusion with application to electron acceleration in the magnetosphere, *J. Geophys. Res.*, *103*, 20,487–20,500.

Tsurutani, B. T., and E. J. Smith (1977), Two types of magnetospheric ELF chorus and their substorm dependences, *J. Geophys. Res.*, *82*, 5112–5128.

Tsyganenko, N. A. (1995), Modeling the Earth's magnetospheric magnetic field confined within a realistic magnetopause, *J. Geophys. Res.*, *100*, 5599–5612.

Tsyganenko, N. A. (1996), Effects of the solar wind conditions on the global magnetospheric configuration as deduced from data-based field models, in *Proceedings of the 3rd International Conference on Substorms (ICS-3), Eur. Space Agency Spec. Publ., ESA SP-389*, 181–185.

Turner, D. L., X. Li, G. D. Reeves, and H. J. Singer (2010), On phase space density radial gradients of Earth's outer-belt electrons prior to sudden solar wind pressure enhancements, *J. Geophys. Res.*, *115*, A01205, doi:10.1029/2009JA014423.

Usanova, M. E., I. R. Mann, I. J. Rae, Z. C. Kale, V. Angelopoulos, J. W. Bonnell, K.-H. Glassmeier, H. U. Auster, and H. J. Singer (2008), Multipoint observations of magnetospheric compression-related EMIC Pc1 waves by THEMIS and CARISMA, *Geophys. Res. Lett.*, *35*, L17S25, doi:10.1029/2008GL034458.

Young, S. L., R. E. Denton, B. J. Anderson, and M. K. Hudson (2002), Empirical model for $\mu$ scattering caused by field line curvature in a realistic magnetosphere, *J. Geophys. Res.*, *107*(A6), 1069, doi:10.1029/2000JA000294.

D. N. Baker and S. R. Elkington, Laboratory for Atmospheric and Space Physics, University of Colorado at Boulder, 1234 Innovation Dr., Boulder, CO 80303, USA.

J. P. McCollough, Space Vehicles Directorate, Air Force Research Laboratory, 3550 Aberdeen Ave. SE, Kirtland Air Force Base, NM 87117, USA. (james.mccollough@us.af.mil)

DISTRIBUTION LIST


DTIC/OCP
8725 John J. Kingman Rd, Suite 0944
Ft Belvoir, VA 22060-6218            1 cy

AFRL/RVIL
Kirtland AFB, NM 87117-5776          2 cys

Official Record Copy
  AFRL/RVBXR/Adrian Wheelock          1 cy